submitted to *The Astrophysical Journal*
Preprint typeset using LaTeX style emulateapj v. 5/2/11

DISCOVERY OF AN ENORMOUS LYα NEBULA IN A MASSIVE GALAXY OVERDENSITY AT $z = 2.3$

Zheng Cai[1,2,11], Xiaohui Fan[2], Yujin Yang[3], Fuyan Bian[4], J. Xavier Prochaska[1], Ann Zabludoff[2], Ian McGreer[2], Zhen-Ya Zheng[5,6], Richard Green[2], Sebastiano Cantalupo[7], Brenda Frye[2], Erika Hamden[8], Linhua Jiang[9], Nobunari Kashikawa[10], Ran Wang[9]

[1] UCO/Lick Observatory, University of California, 1156 High Street, Santa Cruz, CA 95064, USA
[2] Steward Observatory, University of Arizona, 933 North Cherry Avenue, Tucson, AZ, 85721, USA
[3] Korea Astronomy and Space Science Institute, 776 Daedeokdae-ro, Yuseong-gu Daejeon, Korea
[4] Research School of Astronomy & Astrophysics, Mount Stromlo Observatory, Cotter Road, Weston ACT 2611, Australia
[5] Instituto de Astrofisica, Pontificia Universidad Catolica de Chile, 7820436 Santiago, Chile
[6] Chinese Academy of Sciences South America Center for Astronomy, 7591245 Santiago, Chile
[7] Institute for Astronomy, ETH Zurich, Wolfgang-Pauli-Strasse 27, 8093 Zurich, Switzerland
[8] California Institute Technology, 1200 East California Boulevard, Pasadena, CA, USA
[9] The Kavli Institute for Astronomy and Astrophysics, Peking University, Beijing 100871, P. R. China
[10] National Astronomical Observatory of Japan, Mitaka, Tokyo,181-8588, Japan and
[11] Hubble Fellow

submited to The Astrophysical Journal

ABSTRACT

Enormous Lyα Nebulae (ELANe), unique tracers of galaxy density peaks, are predicted to lie at the nodes and intersections of cosmic filamentary structures. Previous successful searches for ELANe have focused on wide-field narrowband surveys, or have targeted known sources such as ultraluminous quasi-stellar-objects (QSOs) or radio galaxies. Utilizing groups of coherently strong Lyα absorptions (CoSLAs), we have developed a new method to identify high-redshift galaxy overdensities and have identified an extremely massive overdensity, BOSS1441, at $z = 2-3$ (Cai et al. 2016a). In its density peak, we discover an ELAN that is associated with a relatively faint continuum. To date, this object has the highest diffuse Lyα nebular luminosity of $L_{\rm nebula} = 5.1 \pm 0.1 \times 10^{44}$ erg s^{-1}. Above the 2σ surface brightness limit of $\mathrm{SB}_{\mathrm{Ly}\alpha} = 4.8 \times 10^{-18}$ erg s^{-1} cm^{-2} arcsec^{-2}, this nebula has an end-to-end spatial extent of 442 kpc. This radio-quiet source also has extended C iv λ1549 and He ii λ1640 emission on $\gtrsim 30$ kpc scales. Note that the Lyα, He ii and C iv emission all have double-peaked line profiles. Each velocity component has a full-width-half-maximum (FWHM) of $\approx 700-1000$ km s^{-1}. We argue that this Lyα nebula could be powered by shocks due to an AGN-driven outflow or/and photoionization by a strongly obscured source.

1. INTRODUCTION

During the peak epoch of galaxy formation at $z = 2-3$ (e.g., Bouwens et al. 2011), most of the baryons in the Universe reside outside galaxies; they lie within the intergalactic medium (IGM) and circumgalactic medium (CGM) (e.g., Cen et al. 1994; Miralda-Escudé et al. 1996; Hernquist et al. 1996; Rauch 1998). The IGM and CGM provide a vast reservoir for fueling the star formation of galaxies and also serve as a "sink" for metals driven from the galactic feedback (e.g., Prochaska et al. 2011; Tumlinson et al. 2011). On the other hand, the properties and structures of the IGM/CGM, such as kinematics, morphology, and metallicity, are increasingly reshaped by the energetic processes occuring in galaxies, and therefore the IGM/CGM acts as a laboratory to stringently constrain the physics of the galaxy formation (e.g., Fumagalli et al. 2011).

Intergalactic/circumgalactic filaments have been studied via QSO absorption lines (e.g., Rauch 1998). But QSO absorption studies are limited due to the sparseness of background QSOs. To reveal the connection of intergalactic gas to galaxies and their circumgalactic medium (i.e. on scales of $\sim$100 kpc), one must constrain the full three-dimensional intergalactic/circumgalactic material using more numerous, but fainter, background galaxy populations (e.g., Lee et al. 2014) or directly map the faint diffuse emission of the intergalactic medium (IGM) or circumgalactic medium (CGM) (e.g., Cantalupo et al. 2014; Martin et al. 2015; Borisova et al. 2016). The Lyα line is the primary coolant of gas with $T \sim 10^4$ K and can be used to trace the CGM/IGM via emission. Such Lyα nebulae provide us an indispensable opportunity to study the CGM in emission.

Theoretical models suggest that several mechanisms may generate circumgalactic Lyα emission: (1) recombination radiation following photoionization (fluorescence) powered by ultraviolet (UV) sources (Gould & Weinberg 1996; Cantalupo et al. 2005; Geach et al. 2009; Kollmeier et al. 2010); (2) cooling radiation due to the gravitationally heated gas (Fardal et al. 2001; Yang et al. 2006; Dijkstra & Loeb 2009; Faucher-Giguère et al. 2010); (3) radiation from shock-heated gas driven by the feedback of galactic outflow (e.g., Villar-Martín et al. 2007; Taniguchi & Shioya 2000; Wilman et al. 2005); and (4) resonant scattering of Lyα from the embedded source (Dijkstra & Loeb 2009; Cantalupo et al. 2014). The photoionization radiation is generated when the dense regions of the CGM are photoionized by strong ionizing sources and then recombine to emit Lyα photons. Cooling radiation is the Lyα photons released when gas settles into galactic potential wells (e.g., Yang et al. 2006). Shock-heating can be powered by supernovae, or by relativistic winds or jets resulting from gas accretion onto supermassive black holes (SMBHs). Lyα resonant scatter-

[1] Email: zcai@ucolick.org

ing produces extended Lyα halos as Lyα photons propagate outward and is characterized by a double-peaked structure of the resonant emission lines (e.g., Yang et al. 2014). These mechanisms are believed to power the extended Lyα emission in high-density regions of the early Universe. The Lyα nebulae/blobs (LABs) are expected to occupy massive dark matter halos ($\sim 10^{13}$ M$_\odot$), representing sites of the most active star formation and tracing large-scale mass overdensities (e.g., Steidel et al. 2000; Prescott et al. 2009; Yang et al. 2009).

A few observational efforts have been made to search for Lyα nebulae/blobs at $z = 2 - 3$. These successful searches include narrowband imaging surveys of random fields (e.g., Steidel et al. 2000; Francis et al. 2001; Palunas et al. 2004; Dey et al. 2005; Yang et al. 2009; Prescott et al. 2009; Yang et al. 2010), narrowband imaging of known overdensities (Matsuda et al. 2005), and targeting biased halo tracers, such as ultraluminous QSOs (e.g., Cantalupo et al. 2014; Hennawi et al. 2015) and radio galaxies (e.g., Heckman et al. 1991; Villar-Martín et al. 2007; Miley & De Breuck 2008). Using VLT/MUSE, Borisova et al. (2016) present a blind survey for Lyα nebulae associated with 17 brightest radio-quiet QSOs at $3 < z < 4$. They find that 100% of the QSOs are associated with Lyα nebulae with linear sizes of $\sim 100 - 320$ kpc. In this sample, the relatively narrow Lyα FWHMs ($300 - 600$ km s^{-1}) are consistent with a fluorescent powering mechanism. Increasing evidence has shown that the Lyα nebulae often lie in regions that contain both enhanced UV-radiation (or nearby UV sources) and gas overdensities (Hennawi & Prochaska 2013; Hennawi et al. 2015).

The extended He II and C IV associated with Lyα nebulae contain crucial information about the powering mechnisms. The extended C IV line allows us to estimate the metallicity of the CGM gas and the size of the metal enriched halos (Arrigoni Battaia et al. 2015). In turn, such metal line emission allows us to examine whether the shocks of the galactic outflow could power the LABs (e.g., Villar-Martín et al. 1999, 2007; Allen et al. 2008; Arrigoni Battaia et al. 2015). Arrigoni-Battaia et al. (2015a) conducted a deep survey of 13 Lyα blobs in the SSA22 overdensity (Steidel et al. 2000; Matsuda et al. 2005), targeting the He II λ1640 and C IV λ1549. These observations did not detect extended He II and C IV emission in any of the LABs, suggesting that photoionization could be a major powering mechanism. Borisova et al. (2016) also did not detect strongly extended He II and C IV emission in their sample of the 17 ultraluminous QSOs, indicating a large fraction of the gas in massive QSO host halos at $z = 3 - 4$ could be cold ($T \sim 10^4$ K) and metal-poor ($Z < 0.1 Z_\odot$). Prescott et al. (2009) detect a LAB that has a spatial extent of 80 kpc at $z \approx 1.67$ associated with extended C IV and He II. The Lyα, C IV, He II and C III]lines all show a coherent velocity gradient of 500 km s^{-1}, strongly indicating a 50 kpc large rotational disk illuminated by an AGN.

Recently, two enormous Lyα nebulae (ELANe) have been discovered to have a large spatial extent of $\gtrsim 400$ kpc (Cantalupo et al. 2014; Hennawi et al. 2015). These ELANe further offer excellent laboratories to detect and map the gas in the dense part of the intergalactic medium (IGM), and to study how the IGM feeds star formation in massive halos (Martin et al. 2014, 2015). Arrigoni Battaia et al. (2015) conducted deep spectroscopic integrations targeting He II and C IV emission and report a null detection, suggesting ELANe are mainly due to AGN photoionization on the cool, metal-poor CGM gas.

In this paper, we report a discovery of another ultraluminous ELAN that resides near the density peak of our newly discovered massive overdensity BOSS1441 at $z = 2.32 \pm 0.02$ (Cai et al. 2016a). This nebula has a projected linear size of ≈ 450 kpc, comparable with the Slug nebula (Cantalupo et al. 2014), and remarkably extended He II and C IV emission over $\gtrsim 30$ kpc. The Lyα, He II and C IV lines all show double-peaked kinematics, with each component having the line widths of 700 $-$ 1000 km s^{-1}. The large spatial extent of Lyα emission, the strongly extended He II and C IV, and the emission line structures and kinematics all make this ELAN unique. This Lyα nebula resides in an overdense field selected utilizing the largest QSO spectral library from the Baryon Oscillations Spectroscopic Survey (BOSS) (e.g., Dawson et al. 2013). It contains a group of extremely rare, high optical depth Lyα absorption (Cai et al. 2015) arising from the IGM overdensity and a rare QSO group (e.g., Cai et al. 2016). We refer to this program as MApping the Most Massive Overdensity Through Hydrogen (MAMMOTH) (Cai et al. 2015). In this paper, we refer this nebula as MAMMOTH-1.

This paper is structured as follows. In §2, we introduce the selection of MAMMOTH-1 and our follow-up observations. In §3, we discuss our observational results. In §4, we discuss the physical properties and several powering mechanisms that could be responsible for such a unique ELAN. We also estimate the cool gas mass. We give a brief summary in §5. We convert redshifts to physical distances assuming a ΛCDM cosmology with $\Omega_m = 0.3$, $\Omega_\Lambda = 0.7$ and $h = 0.70$ (h_{70}). Throughout this paper when measuring distances, we normally refer to physical separations or distances. We use cMpc to represent comoving Mpc, and kpc to represent physical kpc.

2. OBSERVATIONS

2.1. *Target Selection*

MAMMOTH-1 is located in the density peak of the large-scale structure BOSS1441 (Cai et al. 2016a). BOSS1441 was selected because this field contains a group of 5 strong Lyα absorption systems within a 20 h^{-1} comoving Mpc (cMpc) scale at $z = 2.32 \pm 0.03$. Each Lyα absorption has an effective optical depth on a scale of 15 h^{-1} cMpc of $\tau_{\rm eff}^{15h^{-1}{\rm Mpc}} > 3\times$ the mean optical depth ($\langle\tau_{\rm eff}\rangle$). These absorption systems are not due to DLAs. Two of them have $\tau_{\rm eff}^{15h^{-1}{\rm Mpc}} > 4.5 \times \langle\tau_{\rm eff}\rangle$ and the optical depth is higher than the threshold of coherently strong Lyα absorption (CoSLA, see Cai et al. 2016a). This group of absorbers satisfies the selection criteria (a) – (d2) proposed in Cai et al. (2015). The redshift is chosen by our custom narrowband filter *NB403*.

The NB403 filter has a central wavelength of $\lambda_c = 4030$ Å and a bandwidth of FWHM = 45 Å. The NB filter is very efficient to search for the overdensities, because (1) the BOSS QSO density peak lies at $z \sim 2.3$. With a NB filter at a similar redshift, we can fully take advantage of the SDSS Lyα forest survey; (2) The KPNO-

4m/MOSAIC camera is highly sensitive at ~ 4000 Å. In addition, $z \sim 2.3$ is a good redshift for studying galaxy properties using ground-based telescopes. Optical and infrared spectrographs can fully cover the emission lines from Lyα to Hα.

2.2. *KPNO-4m/MOSAIC Narrowband + Broadband Imaging*

After selecting BOSS1441 field, we conducted deep narrowband + broadband imaging and multi-object spectroscopy to select and confirm Lyα emitting galaxies (LAEs). We used the KPNO-4m/MOSAIC-1.1 camera for deep imaging with a custom narrowband filter *NB403* and the Bw broadband filter. These deep imaging observations were designed to reveal LAEs in the BOSS1441 field.

We briefly review our observations in BOSS1441 field. More details can be found in Cai et al. (2016a). The BOSS1441 field was observed on Mar. 2013, Apr. 2014, and Jun. 2014. For the NB403 filter, the total exposure time was 17.9 hours, which consisted of individual 15 or 20 minute exposures with a standard dither pattern to fill in the gaps between the eight MOSAIC CCD chips. The seeing ranged from $1.1'' - 1.7''$, with the median seeing about $1.32''$. For the Bw filter, the total exposure time is 3 hours, which consists of individual 8 minute exposure with fill gap dither pattern. The seeing for taking Bw band ranges from $1.1'' - 1.8''$, with the median value of $1.37''$. Around the LAE density peak region, we discovered strong, highly extended Lyα emission: the ELAN MAMMOTH-1, which is detected in each individual frame with a $15 - 20$ min exposure. The broadband filter (Bw) was observed for total 3 hours to match the depth of narrowband filter. These observing conditions enable us to achieve a narrowband magnitude $m_{\mathrm{NB403}} = 25.1$ at 5σ (aperture: 2.5"), and Bw-band magnitude $m_{\mathrm{Bw}} = 25.9$ at 5σ. This depth corresponds to a 1σ Lyα surface brightness limit of $\mathrm{SB}_{\mathrm{Ly}\alpha} = 2.4 \times 10^{-18}$ erg s^{-1} cm^{-2} arcsec^{-2}.

2.3. *LBT Imaging and Multiobject Spectroscopy*

We used the Large Binocular Camera (LBC) on the Large Binocular Telescope (LBT) to obtain deep imaging using the U, V, and i broadband filters. The LBC imaging enables the selection of the star-forming galaxies at $z \approx 2.3$ (e.g., Adelberger et al. 2005) and helps to eliminate [OII] contaminants using the BX galaxy selection technique.

We also used the Dual channel of the Medium-Dispersion Grating Spectroscopy (MODS) (Byard & O'Brien 2000) on the LBT to spectroscopically confirm the redshifts of galaxies and the Lyα nebula in the BOSS1441 overdense field. The LBT/MODS provides high efficiency over 3200Å – 10,000 Å with a resolution of $R = 2000$. We used a dichroic that divides the incoming beam at ≈ 5700Å. This configuration covers Lyα and a few interstellar lines, e.g., C IV $\lambda 1550$, He II $\lambda 1640$, C III] $\lambda 1907/1909$, for galaxies at $z = 2.3$.

We used a MODS mask to observe the MAMMOTH-1 nebula and other LAEs in the field. The total exposure time was 6 hours. Each mask was split into six 1,800 sec integrations, with a typical seeing of $1''$. The slit length on the MAMMOTH-1 nebula is $10''$ (Figure 1).

The MODS data reduction followed the LBT/MODS reduction routine. First, each raw image was processed with the MODS CCD reduction utilities (modsTools v03) to obtain bias-subtracted and flat-fielded images. We generated polynomial fits to the arc calibration to determine the transformation between image pixels and wavelength. The sky model was fit to each image using B-splines and then subtracted. We used LACOSMIC (Van Dokkum 2010) to identify cosmic rays during the construction of the sky model. The individual exposures were combined with inverse variance weighting to produce the final 2D spectrum.

3. OBSERVATIONAL RESULTS

3.1. *Mapping the Lyα Emission*

In Figure 1, we present the stacked images of MAMMOTH-1 in both the NB403 narrowband and Bw broadband images. We also overplot the LBT/MODS spectral slit. From this figure, we detect extended structures in both the narrowband (NB403, left panel) and broadband images (Bw, right panel). In the Bw broadband, we detect multiple sources associated with the MAMMOTH-1. In Figure 2, we present the continuum subtracted Lyα image. We smooth the image using a Gaussian Kernel with $1''$ (Cantalupo et al. 2014; Hennawi et al. 2015). Within the 2σ (4.8×10^{-18} erg s^{-1} cm^{-2} arcsec^{-2}) surface brightness contour, this ELAN has an end-to-end projected extent of 53 arcsec (442 physical kpc).

In the broadband image, the brightest two sources: brighter source A ($B_{\mathrm{AB}} \approx 23.5$, $i_{\mathrm{AB}} \approx 22.5$) and fainter source B ($B_{\mathrm{AB}} \approx 25.1$, $i_{\mathrm{AB}} \approx 24.3$) are marked in Figure 1. Source B resides in the flux peak of the broadband subtracted narrowband image. Our LBT/MODS spectroscopy shows that source A is a low-redshift AGN at $z = 0.16$, while source B is an object at $z = 2.32$. In Figure 3, we present the 1-D spectrum of source B which has strong emission in Lyα, He II, C IV, and C III]. Using LBT/LBC imaging, we find that source B has a brightness of $U_{\mathrm{AB}} = 25.77 \pm 0.07$, $V_{\mathrm{AB}} = 24.37 \pm 0.03$, $i_{\mathrm{AB}} = 24.30 \pm 0.03$. Although it is difficult to identify all the possible powering sources associated with MAMMOTH-1, source B's location and redshift suggest that it could be the dominant powering source of MAMMOTH-1. We use source B's position as the center of the MAMMOTH-1: $\alpha = 14{:}41{:}27.62$ $\delta = +40{:}03{:}31.44$.

From the broadband-subtracted narrowband image (Figure 2), we measure that MAMMOTH-1 has a total Lyα luminosity of $5.28 \pm 0.07 \times 10^{44}$ erg s^{-1}. Unlike ELANe powered by ultraluminous type-I QSOs, the Lyα emission of MAMMOTH-1 arises mainly from the diffuse nebula rather than from the point-spread function (PSF). In Figure 4, we present the radial profile of MAMMOTH-1's surface brightness. This ELAN has an extremely high extended nebular luminosity, and the central PSF contributes only 4% of the total Lyα luminosity. If we subtract the Lyα PSF (source B in Figure 1), MAMMOTH-1 has an extended nebular Lyα luminosity of $5.07 \pm 0.07 \times 10^{44}$ erg s^{-1}, the highest discovered to date. We summarize the size and luminosity of MAMMOTH-1 in Table 1.

In Figure 2, the northern/eastern part of MAMMOTH-1 seems to have a filamentary structure. If this filamentary structure is real, it aligns the same direction with the morphology of the large-scale structures (see Cai et al. 2016a). In the cosmic hierarchical nature of structure formation, large-scale filaments are formed out of the merging of small-scale pieces. Simulations suggest that cosmic webs containing baryonic matter tend to align with underlying large-scale structures of dark matter (e.g. Cen et al. (1994); Cen & Ostriker (2006); Fukugita & Peebles (2004), Colberg et al. 2005, Hellwing 2014). Our observations tentatively support these simulations.

3.2. *Emission Line Profiles*

The deep LBT/MODS spectra reveal Lyα, He II, C IV, and C III] emission (Figure 4). Both C IV and He II extend over $\gtrsim$ 30 kpc scales (Figure 5). Extended He II and C IV have been observed previously in radio galaxies, but MAMMOTH-1 is unlikely to be powered by radio jet. From the FIRST radio catalog (Becker et al. 1995), we do not find any radio-loud sources with a radio flux at 1.4 GHz $F(1.4\mathrm{GHz}) > 0.9$ mJy in the area within 30 arcsec of the MAMMOTH-1 nebula. We use the redshift of the non-resonant He II $\lambda1640$ line as the redshift of MAMMOTH-1, yielding $z = 2.319 \pm 0.004$.

The Lyα, C IV, and He II line profiles reveal two main components. In Figure 5, we fit these lines with two Gaussians. For the Lyα line, the blue component has a best-fit FWHM of 876 ± 120 km s^{-1} and the red component has a best-fit FWHM of 1140 ± 160 km s^{-1}. The redshift offset between the two components is ≈ 700 km s^{-1}. For the He II line, the blue component has a FWHM of 714 ± 100 km s^{-1}, and the red component has a best-fit FWHM of 909 ± 130 km s^{-1}. The offset between the two components is the same as that of Lyα.

3.3. *Flux and Surface Brightness*

In our LBT/MODS spectra, the slit is $10''$ long and $2''$ wide. We measure the flux of Lyα, He II, C IV, and C III]. The aperture we applied is 15 ±5 kpc ($1.8\pm0.6''$) away from source B along the slit direction, and within 3000 km s^{-1} in the wavelength direction (see blue rectangle in Figure 5), sufficiently large to include all the diffuse emission in the wavelength direction. This gives a size of $2''$ (slit width) $\times 1.2''$ (along the slit direction). We apply this aperture to measure the surface brightness of the emission lines. We regard the flux as the CGM emission at $R = 1.8''$ (15 kpc) away from the central source.

Applying this aperture to the LBT/MODS 2D spectrum (Figure 5), we determine that the Lyα emission (first panel) has a flux of $f_{\mathrm{Ly}\alpha,15\mathrm{kpc}} = 6.6 \pm 0.2 \times 10^{-16}$ erg s^{-1} cm^{-2}, corresponding to $L_{\mathrm{Ly}\alpha,15\mathrm{kpc}} = 1.7 \times 10^{43}$ erg s^{-1}. The surface brightness of Lyα is $\mathrm{SB}_{\mathrm{Ly}\alpha,15\mathrm{kpc}} = 2.99 \pm 0.01 \times 10^{-16}$ erg s^{-1} cm^{-2} arcsec^{-2}.

The extended He II emission (second panel of Figure 5) has a line flux of $f_{\mathrm{HeII},15\mathrm{kpc}} = 7.8 \pm 0.2 \times 10^{-17}$ erg s^{-1} cm^{-2}, corresponding to a luminosity of $L_{\mathrm{HeII},15\mathrm{kpc}} = 3.2 \pm 0.1 \times 10^{42}$ erg s^{-1}, and a surface brightness $SB_{\mathrm{HeII},15\mathrm{kpc}} = 3.3 \pm 0.1 \times 10^{-17}$ erg s^{-1} cm^{-2} arcsec^{-2}.

The extended C IV emission (third panel of Figure 5) has a line flux of $f_{\mathrm{CIV},15\mathrm{kpc}} = 8.8 \pm 0.2 \times 10^{-17}$ erg s^{-1} cm^{-2}, corresponding to $L_{\mathrm{CIV},15\mathrm{kpc}} = 3.6 \pm 0.1 \times 10^{42}$ erg s^{-1} and $SB_{\mathrm{CIV},15\mathrm{kpc}} = 3.7 \pm 0.1 \times 10^{-17}$ erg s^{-1} cm^{-2} arcsec^{-2}.

The C III] emission (fourth panel of Figure 5) has a line flux of $f_{\mathrm{HeII},15\mathrm{kpc}} = 0.9 \pm 0.2 \times 10^{-17}$ erg s^{-1} cm^{-2}, corresponding to $L_{\mathrm{HeII},15\mathrm{kpc}} = 0.4 \pm 0.1 \times 10^{42}$ erg s^{-1} and $SB_{\mathrm{HeII},15\mathrm{kpc}} = 0.4 \pm 0.1 \times 10^{-17}$ erg s^{-1} cm^{-2} arcsec^{-2}. We summarize our surface brightness measurements in Table 2.

3.4. *Comparison between MAMMOTH-1 and Other Lyα Nebulae*

In Figure 6, we present the sizes and Lyα luminosities for different Lyα nebulae from the literature in comparison with MAMMOTH-1. The Lyα emission from the central source has also been included. The typical size measurements for these objects are above surface brightness contours of $\sim 5 \times 10^{-18}$ erg s^{-1} cm^{-2} arcsec^{-2}, comparable to our measurements for MAMMOTH-1, which are above 4.8×10^{-18} erg s^{-1} cm^{-2} arcsec^{-2}. If we restrict the size measurements to the surface brightness coutour of 4.8×10^{-18} erg s^{-1} cm^{-2} arcsec^{-2}, MAMMOTH-1 has a similar size to the Slug nebula (Cantalupo et al. 2014). But note that Cantalupo et al. (2014) reached a factor of $3\times$ deeper than our current narrowband imaging, so MAMMOTH-1 nebula may be extended on an even larger scale in deeper data. In Table 3, we further compare the diffuse nebular luminosities (with excluding the PSF contribution). MAMMOTH-1 has the highest diffuse nebular luminosity among all the confirmed Lyα nebulae and ELANe.

4. DISCUSSION

In the previous section, we showed that the ELAN MAMMOTH-1 has a Lyα spatial extent of ≈ 440 kpc and a total luminosity of $5.28 \pm 0.07 \times 10^{44}$ erg s^{-1}. This nebula resides in an extremely overdense galaxy environment previously discovered at $z = 2.3$. Moreover, this radio-quiet nebula has the strongly extended He II, C IV, and C III]emission (Figure 4). The Lyα, He II, C IV line profiles are all double-peaked. In Table 3, we compare the properties of MAMMOTH-1 to other ELANe recently discovered. The Lyα spatial extent and the strong emission of C IV and He II make MAMMOTH-1 unique. In this section, we derive the physical properties of MAMMOTH-1, and we discuss several possible physical explanations for powering this ELAN.

4.1. *Ionizing Radiation*

A comparison between hydrogen ionizing photons and helium ionizing photons constrains the hardness of the ionizing radiation. The number of H$^+$ ionizing photons can be expressed as:

$$Q(\mathrm{H}) = \frac{\mathrm{L}_{\mathrm{Ly}\alpha,15\mathrm{kpc}}}{\mathrm{h}\nu_{\mathrm{Ly}\alpha}} \frac{1}{0.68} \approx 1.5 \times 10^{54}\ \mathrm{s}^{-1} \qquad (1)$$

where $f_{\mathrm{Ly}\alpha,15\mathrm{kpc}} = 2.99 \pm 0.01 \times 10^{-16}$ erg s^{-1} cm^{-2}, corresponding to $L_{\mathrm{Ly}\alpha,15\mathrm{kpc}} = 1.7 \times 10^{43}$ erg s^{-1}. We have assumed that $\approx 68\%$ of the ionizing photons are converted into Lyα emission (Spitzer 1978). This is a lower limit of Lyα, because it may be destroyed by dust.

Using the same spatial region, we measured that the He II emission has a flux of $f_{\mathrm{HeII}} = 7.8 \pm 0.2 \times 10^{-17}$ erg s^{-1} ($L_{\mathrm{HeII}} = 3.2 \pm 0.1 \times 10^{42}$ erg s^{-1}). We calculated the He$^+$-ionizing photon number ($E_\nu \geq 54.4$ eV) using the

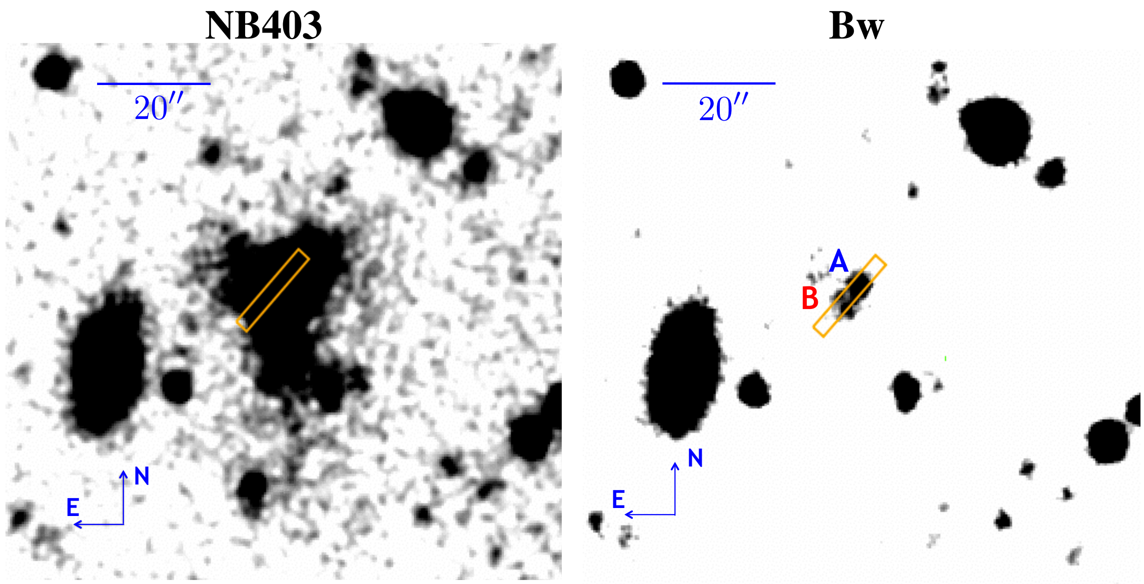

FIG. 1.— Final stacked images of the field surrounding MAMMOTH-1 overplotted with our LBT/MODS slit (orange rectangle). Each image has an area of 80″ centered on the Lyα nebula. The narrow-band (NB403) image (left panel) at the Lyα line of the redshift of MAMMOTH-1 ($z = 2.32$). The deep Bw-band image (middle panel) does not show any extended emission associated with MAMMOTH-1. We put the spectral slit (orange slit) containing the brightest two sources (A, B) in the center of MAMMOTH-1.

equation of:

$$Q(\mathrm{He}^{+}) = \frac{\mathrm{L}_{\lambda 1640}}{\mathrm{h}\nu_{\lambda 1640}} \frac{\alpha^{\mathrm{eff}}_{\mathrm{HeII}}}{\alpha^{1640}_{\mathrm{HeII}}} \approx 2.8 \times 10^{53}\ \mathrm{s}^{-1} \qquad (2)$$

where we assumed the case B recombination model, with a temperature of $T = 10^4$ K. Under this assumption, $\alpha^{\mathrm{eff}}_{\mathrm{HeII}}(T) = 1.53 \times 10^{-12}$ cm^3 s^{-1} (Prescott et al. 2009). Therefore Q(He$^+$)/Q(H) is equal to 0.19. Note this is an upper limit for the Q(He$^+$)/Q(H) ratio because Lyα could be destroyed by dust. The Q(He$^+$)/Q(H) ratio suggests that the powering source of MAMMOTH-1 produces a hard ionizing radiation spectrum. In comparison, if we assume a typical Pop II stellar population with a Salpeter IMF, and a low metallicity of $Z = 10^{-4}\ Z_{\odot}$, then Q(He$^+$)/Q(H) equals 0.005 (Schaerer 2003; Prescott et al. 2009), two orders of magnitude smaller than the value we estimated from MAMMOTH-1. This hard ionization ratio could arise because of significantly lower metallicity (e.g., Population III), a stellar population with a top-heavy IMF (Tumlinson et al. 2003; Schaerer 2003; Cai et al. 2011), or an AGN. The detection of strong C IV and C III] emission make this nebula unlikely to be powered by a low metallicity (e.g., Pop III) stars. Our current data support the conclusion that this ELAN is powered by one or more hard ionizing sources (e.g., AGN).

4.2. *Sources of the enormous Lyα, strong extended C IV, and He II emission in a radio-quiet system*

At least 15 Lyα nebulae with Lyα spatial extents larger than 150 kpc have recently been discovered (e.g., Cantalupo et al. 2014; Hennawi et al. 2015; Borisova et al. 2016). But in none of these nebulae have strongly extended He II and C IV been reported. We will discuss below several mechanisms that may power MAMMOTH-1.

4.2.1. *Photoionization Model*

In photoionization models, C IV emission is mainly powered by collisional excitation (e.g., Arrigoni Battaia et al. 2015). The intensity of collisional excitation has a strong dependence on the temperature (e.g., Gurzadyan 1997). A higher ionization parameter (U) yields a higher gas temperature, and thus the C IV intensity strongly depends on the ionization parameter. Collisional excitation also depends on the gas density and column density of C IV. The He II emission is mainly due to recombination. The fraction of He II emission reaches a peak at $U \sim -2.0$, where a larger fraction of the helium has been doubly ionized (e.g., Arrigoni-Batta et al. 2015b). Higher ionization parameters only modestly change the He II intensity. The C III] emission increases with the ionization parameter, and it is also highly sensitive to the metallicity. The C III] emission peaks at a gas metallicity of $Z \sim 0.2 \times Z_{\odot}$, and it decreases at both higher and lower metallicities (Erb et al. 2009). Therefore, the combination of He II, C IV, and C III] strongly constrains the physical properties of the CGM.

Using CLOUDY ionization modeling (Ferland 1996), Arrigoni Battaia et al. (2015) have thoroughly investigated the He II/ Lyα and C IV/Lyα ratios under different ionization parameters, gas densities (n_{H}), and QSO ionizing luminosities ($L_{\nu_{\mathrm{LL}}}$) for the Slug nebula and nebulae in SSA22 protocluster. In §3, we suggest that MAMMOTH-1 could be powered mainly by source B. Source B may be a strongly obscured source, e.g., a type-II AGN. The Lyα emission from a strongly obscured source may be complicated to interpret. In this section, we conduct a similar studies as Arrigoni Battaia et al. (2015), but focus on reproducing the He II surface brightness and the C IV/He II and C III]/He II line ratios. In our CLOUDY modeling, the AGN continuum follows the recipe in Matthews & Ferland

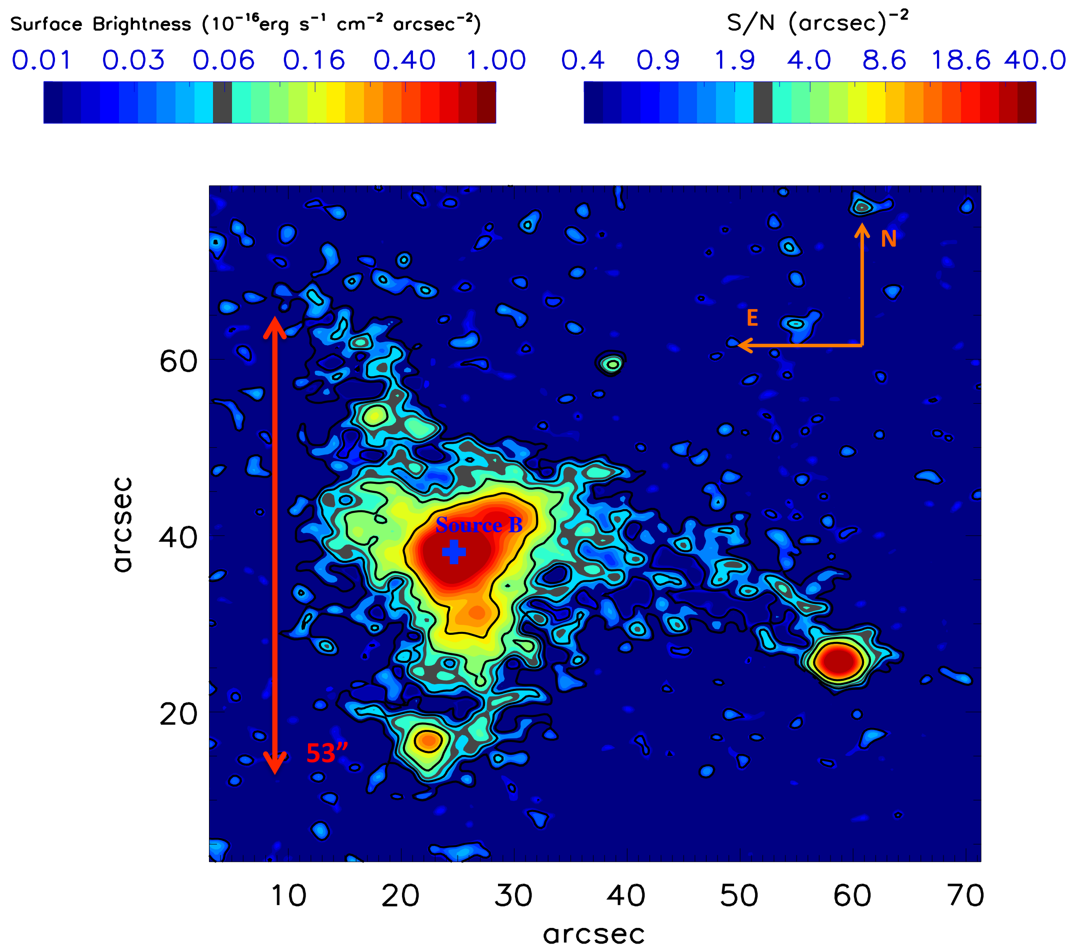

FIG. 2.— Continuum-subtracted, smoothed narrow-band image of the field around the enormous Lyα nebula (ELAN) MAMMOTH-1. The color map and contours indicate the Lyα surface brightness (left color bar) and the signal-to-noise ratio per arcsec^2 aperture (right color bar), respectively. This image reveals the Lyα emission of the enormous Lyα nebula (ELAN). The current 1σ surface brightness limit is 2.4×10^{-18} erg s^{-1} cm $^{-2}$ arcsec^{-2}. Above the flux contour of $SB > 4.8 \times 10^{-18}$ erg s^{-1} cm^{-2} arcsec^{-2}, MAMMOTH-1 has a total luminosity of $L = 5.28 \pm 0.07 \times 10^{44}$ erg s^{-1}. Further, we tentatively detect filamentary structures around MAMMOTH-1.

(1987). We assume that the CGM clouds have a constant hydrogen density ($n_{\rm H}$). We assume that the emitting gaseous clouds are uniformly distributed throughout the halo, and we further assume a standard plane-parallel geometry for these clouds. To match our measurements in §3.3, we assume that the distance between the CGM cloud and the central QSO is $R \approx 15$ kpc. In our CLOUDY models, we try combinations of different $n_{\rm H}$ values, with $n_{\rm H} = 0.01 - 10.0$ cm^{-3} (steps of 0.5 dex); different ionization parameters, with Log $U = -3 - 1$ (steps of 0.5 dex); different column densities of $N_{\rm H} = 10^{19} - 10^{22}$ cm^{-2} (steps of 0.5 dex), and metallicities with $Z = 0.1 - 1.0 \times Z_\odot$ (steps of $0.5 \times Z_\odot$). We assume a gas covering fraction of $f_C = 0.3$ (e.g., Cantalupo et al. 2014).

Our observed He II surface brightness is $SB_{\rm HeII} \approx 3.3 \times 10^{-17}$ erg s^{-1} cm^{-2} arcsec^{-2}. We require that the parameter combinations yield a He II surface brightness of $\approx 3.0 - 3.5 \times 10^{-17}$ erg s^{-1} cm^{-2} arcsec^{-2} to roughly match the observed He II emission. In Figure 7, we present models that yield the observed He II surface brightness, and present our observed value using a red dot with an error bar. Using the parameter combinations with ($N_{\rm H}$, Z, Log(U), $n_{\rm H}$)= (10^{20} cm^{-2}, 0.5 $Z_\odot$, -2, 0.1 cm^{-3}) and (10^{18} cm^{-2}, 1.0 $Z_\odot$, -2, 2.0 cm^{-3}) reproduce the observed intensities of He II, C IV and C III], and the line ratios of C IV/He II and C III]/He II within 1σ errors (red error bars in Figure 7). Therefore, the C IV/He II and C III]/He II line ratios are consistent with AGN photoionization.

4.2.2. *Resonant Scatter*

In §3, we have shown that the Lyα, C IV and He II emission line profiles contain at least two major components. Double-peaked Lyα emission is predicted by the resonant scattering of Lyα photons (e.g. Dijkstra et al. 2006; Yang et al. 2014). The key prediction of these radiative transfer (RT) calculations is that the Lyα spectrum is double peaked with an enhanced blue peak, producing a blueshift of the Lyα profile. Although it is true that

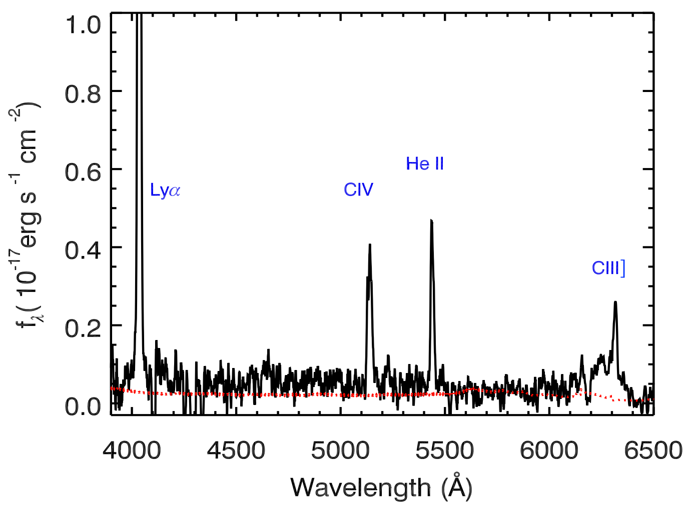

FIG. 3.— The LBT/MODS spectrum of the enormous Lyα nebula (ELAN) MAMMOTH-1 at $z = 2.32$ centered on source B in Figure 1. This spectrum is taken using a long-slit with a $2''$ slit width. The red dotted line represents the error of the spectrum.

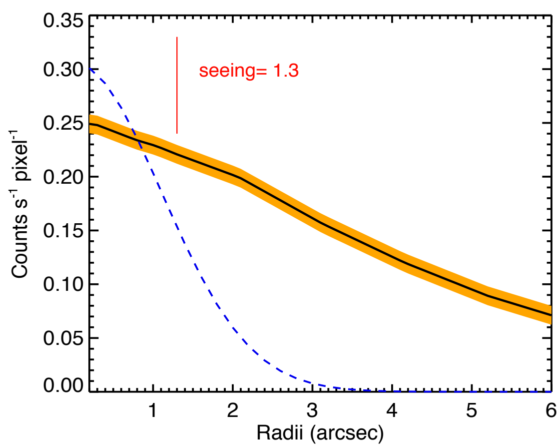

FIG. 4.— Surface brightness as a function of radii. MAMMOTH-1 has a very extended profile (black line). Orange present the 1-σ error of the radial profile. We use source B's position (Figure 1) as the center of MAMMOTH-1. Blue dashed line represents central point-spread-function (PSF). The PSF is constructed using a full-width-half-maximum (FWHM) that is equal to the seeing of 1.3". The amplitutde is determined assuming all of the ELAN's luminosity within the Moffat FWHM is contributed by the PSF. The central PSF constitutes only 4% of entire flux of MAMMOTH-1.

this prediction matches the Lyα profile of MAMMOTH-1, the He II emission has the same double-peaked structure as Lyα. He II is an optically-thin, non-resonant emission line whose photons escape the halo without radiative transfer effects (e.g., Yang et al. 2014). The non-resonant, optically thin emission lines should directly reflect the spatial distribution and kinematics of the gas. Thus, the emission-line structure of He II strongly suggests that the double peaks are due to the actual kinematics (e.g., gas flows) rather than the radiative transfer effects.

4.2.3. *Shocks due to a Gas Flow*

The shocks due to flowing gas can also explain the double peaks of the emission lines. If the fast wind of an outflow is launched, then the shock could heat the surrounding interstellar gas over scales of $\gtrsim 50$ kpc (Debuhr et al. 2012; Harrison et al. 2014). Current galaxy formation simulations and observations suggest that high-velocity ($v_{\rm max} \sim 1000$ km s^{-1}) galactic outflow can quench star formation in the most massive galaxies and eject heavy elements into the IGM (e.g., Taniguchi & Shioya 2000; Martin 2005; Ho et al. 2014). Such galactic winds can be driven by (1) intense star formation or (2) relativistic winds or jets resulting from the gas accretion onto the supermassive black holes (e.g., Leitherer et al. 1999; Tombesi et al. 2015).

Wilman et al. (2005) find a Lyα blob at $z = 3.09$ in the SSA22 overdensity (Steidel et al. 2000; Matsuda et al. 2005) whose double-peaked line profile is consistent with a simple outflow model. This model suggests that the Lyα emission is absorbed by a foreground shell of neutral gas that is pushed out up to a $\approx$ 70 kpc by an AGN-driven outflow. Using MAPPINGS (Dopita & Sutherland 1996) and CLOUDY (Ferland 1996) modeling, Villar-Martín et al. (1999, 2007) and Moy & Rocca-Volmerange (2002) suggest both shocks and AGN photoionization could power the extended Lyα, He II, and C IV observed in radio galaxies. Using hydrodynamical simulations, Cabot et al. (2016) further argue that the Lyα, He II and C IV emission in $z \approx 3$ Lyα blobs could be primarily due to the shocks. Integral Field Spectrometer (IFS) observations suggest that the high-velocity ($v_{\rm max} \approx 1000$ km s^{-1}) [OIII] outflows exist in a sample of 5 radio-quiet ULIRGs at $z \gtrsim 2$. Such [OIII] outflows are consistent with the AGN-driven wind scenario (e.g., Alexander et al. 2010; Harrison et al. 2012).

MAMMOTH-1 has C III]/He II and C IV/He II line ratios consistent with both photionization and shock models (see Figure 2 and Figure 3 of Villar-Martin et al. 1999). Further, the C IV/Lyα and He II/Lyα ratios of MAMMOTH-1 are consistent with the predictions using shock models (Arrigoni Battaia et al. 2015), with a gas denisty $n_H \sim 0.1 -$ 1 cm^{-3} and a shock velocity of 500 – 600 km s^{-1}. If the extended He II and C IV are powered by shocks due to an AGN-driven outflow, then the double velocity peaks of emission lines can be naturally interpreted. Like Harrison et al. (2014), we draw a schematic diagram to illustrate the outflow interpretation of the extended C IV and He II (Figure 8). The velocity offsets between the two components and the spatial extent of emission lines strongly depend on the orientation of the outflow with respect to the line of sight: if the axis of the outflow is oriented along the line of sight, then a high-velocity offset and a small spatial extent should be observed; and conversely, if the axis of the outflow is in the plane of the sky, then a small velocity offset and a large spatial extent should be observed.

From §3.2, the offset between two velocity components is $\approx$ 700 km s^{-1}. These line structures are similar to ULIRG sample in Harrison et al. (2012). If we assume the extended C IV and He II are due to the AGN outflow, then we can estimate the energy of the outflow:

$$\dot{E} \approx 1.5 \times 10^{46} \; r_{10}^2 \; v_{1000}^3 \; n_{0.5} \; \mathrm{erg\ s}^{-1} \tag{3}$$

where v_{1000} is the velocity offset between two components in units of 1000 km s^{-1}. r_{10} is the radius of the observed of C IV emission in units of 10 kpc. The ambient density is the gas density ahead of the expanding bubble, in the units of 0.5 cm^{-3}. For MAMMOTH-1, if

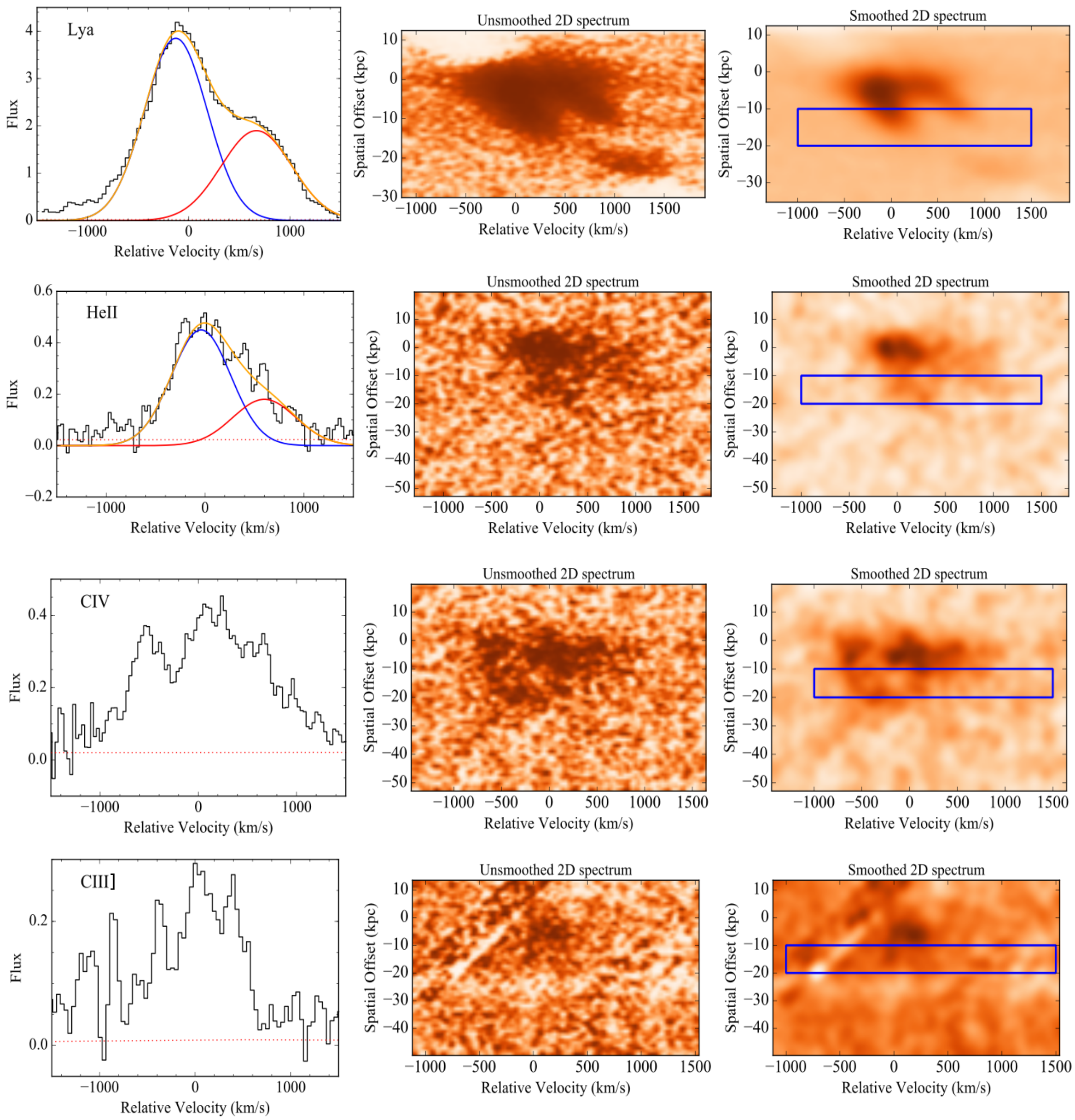

FIG. 5.— The spectrum of emission lines of MAMMOTH-1 observed in LBT/MODS. From top to bottm: Lyα, He II, C IV, and C III]. *Left column:* 1-D zoom of line profiles of Lyα, He II, C IV, and C III] (from top to bottom) as a function of the rest-frame velocity centered on the redshift of the nebula, measured from the He II line. We use two Gaussian functions to fit the two major components of Lyα and He II. Our spectral resolution is $R \approx 1000$ for this slit ($2''$ wide), corresponding to 91 km s^{-1} in the rest-frame of MAMMOTH-1. The measured FWHM for each component is much wider than the spectral resolution. The deviation of C III] emission in the left wing is due to imperfect sky subtraction. *Middle column:* The unsmoothed 2D spectra of Lyα, He II, C IV, and C III]. *Right column:* The 2×2-pixel smoothed spectra of Lyα, He II, C IV, and C III]. From the spectrum, the extended Lyα emission lies the spatial direction along the slit (10"). The C IV extends 33 physical kpc, and He II extends 31 physical kpc. The C III] is on a much smaller scale than C IV and He II. We show the aperture for measuring the surface brightness (blue rectangles).

we assume that the extended C IV and He II are completely powered by an AGN outflow, and further assume that the axis of the outflow is oriented 45 degrees with respect to the sight line, then $r_{10} = 2$, $v_{1000} = 0.7$. Taking these numbers into Equation (3), we establish that the spatially extended outflow in MAMMOTH-1 is potentially injecting energy into the circumgalactic medium at a considerable rate of $2 \times 10^{45-46}$ erg s^{-1}. Over a typical AGN duty cycle of 30 Myr (e.g., Hopkins et al. 2005; Harrison et al. 2012), the total energy injected reaches the order of 10^{60-61} erg. According to Nesvadba et al. (2006), the typical binding energy of a massive elliptical galaxy with a halo mass of $M_{\rm halo} \approx 10^{12}$ M$_\odot$ is about 10^{60} erg. Thus, if MAMMOTH-1 is powered by an AGN outflow, then the outflow energy could be comparable or even an order of magnitude higher than this binding energy, making a vast AGN outflow possibly plays a major role in heating the ISM.

It has also long been suggested that jet-induced shocks can power extended metal-line emission, and extended C IV emission has been reported in a few radio-galaxies with strong radio continua (e.g., McCarthy 1993; Villar-

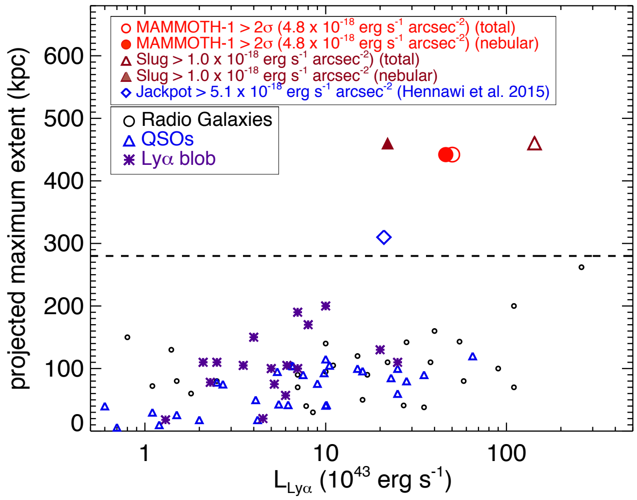

FIG. 6.— Projected maximum extent versus total Lyα luminosity for different objects from the literature. The typical size measurement is above a surface brightness contour of 5×10^{-18} erg s^{-1} cm^{-2} arcsec^{-2}. If we restrict the size measurement to contours above 4.8×10^{-18} erg s^{-1} cm^{-2} arcsec^{-2}, our target MAMMOTH-1 is one of the most extended sources, with a comparable spatial extent to the Slug nebula. The open circle represents the total Lyα luminosity of MAMMOTH-1 and the filled circle represents the nebular luminosity, with excluding the contribution from the central point spread function (PSF). The luminosities of Slug nebula are cited from Cantalupo et al. (2014). The black dashed line shows the virial diameter of a dark matter halo of mass $M \sim 10^{12.5}\ M_{\odot}$, the typical host of radio-quiet QSOs (Martin et al. 2012, Cantalupo et al. 2014).

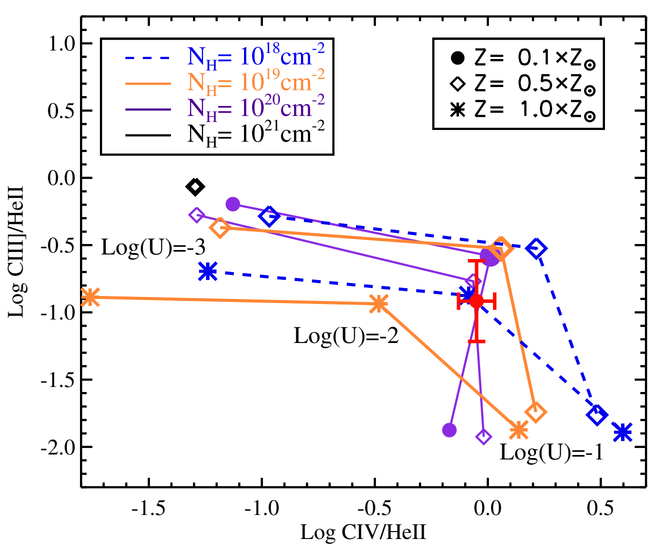

FIG. 7.— Simulation of the intensity ratios of C IV/He II and C III]/He II powered by AGN. Colors represent different ionization parameters ($LogU$) and symbols represent different metallicities of the gaseous clouds. The observed value is marked with red points with an error bar. MAMMOTH-1 is consistent with the photoionization scenario, with an ionization parameter of Log U ≈ 2 and a gas metallicity of 0.1 $Z_{\odot}$.

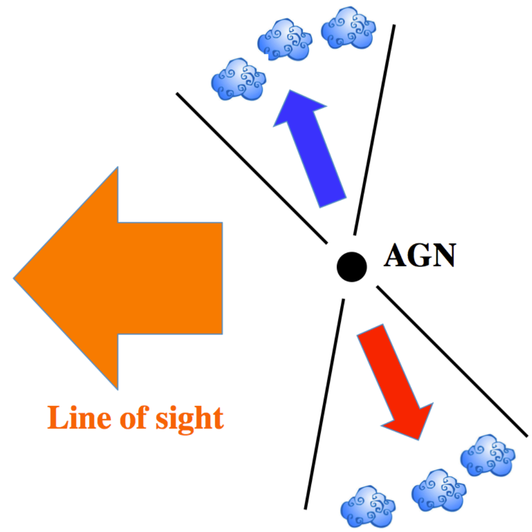

FIG. 8.— A schematic diagram to demonstrate the outflow interpretation of the data. The C IV and He II velocity offsets between the two components and the spatial extent of emission lines shown in Figure 5 strongly depend on the orientation of the outflow with respect to the line of sight. For a given AGN outflow, if the axis of the outflow is oriented along the line of sight, high-velocity offsets and a small spatial extent would be observed. Conversely, if the axis of the outflow is in the plane of the sky, a small velocity offset and a large spatial extent would be seen.

Martín et al. 2007). We argue that our current data disfavour the model of jet-ISM interaction. From the FIRST radio catalog (Becker et al. 1995), we do not find any source with a radio flux at 1.4 GHz $> 0.9\mu$Jy within a radius of 30 arcsec from MAMMOTH-1. Assuming a radio spectrum $S(\nu) \propto \nu^{-0.8}$, this 3-$\sigma$ upper limit corresponds to a luminosity density of $< 3.2 \times 10^{32}$ erg s^{-1} Hz^{-1} at rest-frame 1.4 GHz (Yang et al. 2009). This limit is two orders of magnitude lower than the radio continua of other Lyα nebulae powered by radio galaxies (e.g., Carilli et al. 1997; Reuland et al. 2003).

4.2.4. *Gravitational Cooling Radiation*

Theoretical studies have suggested that Lyα nebula could result from the gravitational cooling radiation (e.g., Haiman & Rees 2001; Dijkstra et al. 2006; Yang et al. 2006; Faucher-Giguère et al. 2010; Rosdahl & Blaizot 2012). Several studies have predicted the He II cooling radiation using hydrodynamical simulations. Yang et al. (2006) predict that the He II line has the FWHM $\lesssim 400$ km s^{-1} even for the most massive halo at $z \approx 2$ ($M \sim 10^{14}\ M_{\odot}$). If our observed He II line profile has two major velocity components as shown in Figure 5, then the He II has a large FWHM of 714 ± 100 km s^{-1} for the blue component and 909 ± 130 km s^{-1} for the red component. The observed FWHMs are much wider than the predicted line width for cooling radiation. Also, using hydrodynamical simulations, Fardal et al. (2001) and Yang et al. (2006) point out that the He II regions should be centrally-concentrated and the He II cooling radiation may be too small to resolve using current ground-based telescopes. This size prediction of the He II cooling radiation does not fit our observations. We have detected extended He II emission over $\gtrsim 30$ kpc scale. Further, if the Lyα emission results from the cooling inflow of the pristine gas in the intergalactic filaments, then we should expect no extended C IV being detected (e.g., Yang et al. 2006; Arrigoni Battaia et al. 2015). Therefore, we conclude that our current observations do not fit with the cooling radiation picture.

5. SUMMARY

In this paper, we present our discovery of an enormous Lyα nebula (ELAN) MAMMOTH-1 at $z = 2.319$ in the density peak of the large-scale structure BOSS1441 (Cai et al. 2016a). Above the 2σ surface brightness contour, this object has the highest nebular luminosity discovered to date: $L_{\mathrm{Ly}\alpha} = 5.1 \pm 0.1 \times 10^{44}$ erg s^{-1} (excluding the Lyα PSF, see §3). Above the 2σ surface brightness limit of $\mathrm{SB}_{\mathrm{Ly}\alpha} = 4.8 \times 10^{-18}$ erg s^{-1} cm^{-2} arcsec^{-2}, we measure this nebula to have an end-to-end spatial extent of ~ 442 kpc, comparable to the largest known Lyα nebula (e.g., Cantalupo et al. 2014).

MAMMOTH-1 is associated with a relatively faint source in the broadband (source B, Figure 1). This source has an extended He II and C IV emission in our LBT/MODS spectra (Figure 5). No radio sources are detected from the FIRST radio catalog (Becker et al. 1995) within 30$''$ from the center of MAMMOTH-1 (§3). Both C IV and He II have a spatial extent of $\gtrsim 30$ kpc. The Lyα, He II and C IV emission all contain two major components, with velocity offsets of ≈ 700 km s^{-1} (§4.2). The large spatial extent of the Lyα, extended He II and C IV emission, and double-peaked line profiles make MAMMOTH-1 to be unique compared to all the ELANe discovered up to date.

We discussed several explanations for MAMMOTH-1. We consider different scenarios including the photoionization (§4.2.1), resonant scattering (§4.2.2), shocks due to gas flows (§4.2.3), and cooling radiation (§4.2.4). We ruled out resonant scattering and cooling radiation as unlikely. Our current data support photoionization (Figure 8) or/and shocks due to the galactic outflow as the source of the extended Lyα emission. The outflow model could naturally generate the double-peaked structures of the He II and C IV emission. The future Integral Field Spectroscopy can examine if this ELAN is powered by a group of galaxies, and also can help us to better understand the nature of MAMMOTH-1.

Acknowledgements: ZC acknowlendges the valuable comments from Fabrizio Arrigoni Battaia, Joe Hennawi and Arjue Dey. ZC, XF, and IM thank the support from the US NSF grant AST 11-07682. ZC and JXP acknowledge support from NSF AST-1412981. AZ acknowledges support from NSF grant AST-0908280 and NASA grant ADP-NNX10AD47G. SC gratefully acknowledges support from Swiss National Science Foundation grant PP00P2_163824. NK acknowledges supports from the JSPS grant 15H03645. Based on observations at Kitt Peak National Observatory, National Optical Astronomy Observatory (NOAO Prop. ID: 2013A-0434; PI: Z. Cai; NOAO Prop. ID: 2014A-0395; PI: Z. Cai), which is operated by the Association of Universities for Research in Astronomy (AURA) under cooperative agreement with the National Science Foundation. The authors are honored to be permitted to conduct astronomical research on Iolkam Du'ag (Kitt Peak), a mountain with particular significance to the Tohono O'odham. The LBT is an international collaboration among institutions in the United States, Italy and Germany. The LBT Corporation partners are: The University of Arizona on behalf of the Arizona university system; Istituto Nazionale di Astrofisica, Italy; LBT Beteiligungsgesellschaft, Germany, representing the Max Planck Society, the Astrophysical Institute Potsdam, and Heidelberg University; The Ohio State University; The Research Corporation, on behalf of The University of Notre Dame, University of Minnesota and University of Virginia.

REFERENCES

Adelberger, K. L., Shapley, A. E., Steidel, C. C., et al. 2005, ApJ, 629, 636
Allen, M. G., Groves, B. A., Dopita, M. A., Sutherland, R. S., & Kewley, L. J. 2008, ApJS, 178, 20-55
Alexander, D. M., Swinbank, A. M., Smail, I., McDermid, R., & Nesvadba, N. P. H. 2010, MNRAS, 402, 2211
Arrigoni Battaia, F., Yang, Y., Hennawi, J. F., et al. 2015, ApJ, 804, 26
Arrigoni Battaia, F., Hennawi, J. F., Prochaska, J. X., & Cantalupo, S. 2015, ApJ, 809, 163
Byard, P. L., & O'Brien, T. P. 2000, Proc. SPIE, 4008, 934
Becker, R. H., White, R. L., & Helfand, D. J. 1995, ApJ, 450, 559
Borisova, E., Cantalupo, S., Lilly, S. J., et al. 2016, arXiv:1605.01422
Bouwens, R. J., Illingworth, G. D., Oesch, P. A., et al. 2011, ApJ, 737, 90
Bond, J. R., Kofman, L., & Pogosyan, D. 1996, Nature, 380, 603
Cai, Z., Fan, X., Jiang, L., et al. 2011, ApJ, 736, L28
Cai, Z., Fan, X., Noterdaeme, P., et al. 2014, ApJ, 793, 139
Cai, Z., Fan, X., Jiang, L., et al. 2015, ApJ, 799, L19
Cai, Z., Fan, X., Peirani, S., et al. 2015, arXiv:1512.06859
Cai, Z., Fan, X., Bian, F., et al. 2016, arXiv:1609.02913
Cabot, S. H. C., Cen, R., & Zheng, Z. 2016, arXiv:1603.09696
Cantalupo, S., Porciani, C., Lilly, S. J., & Miniati, F. 2005, ApJ, 628, 61
Cantalupo, S., & Porciani, C. 2011, MNRAS, 411, 1678
Cantalupo, S., Arrigoni-Battaia, F., Prochaska, J. X., Hennawi, J. F., & Madau, P. 2014, Nature, 506, 63
Carilli, C. L., Röttgering, H. J. A., van Ojik, R., et al. 1997, ApJS, 109, 1
Cen, R., Miralda-Escudé, J., Ostriker, J. P., & Rauch, M. 1994, ApJ, 437, L9
Dawson, K. S., Schlegel, D. J., Ahn, C. P., et al. 2013, AJ, 145, 10
Davis, M., Efstathiou, G., Frenk, C. S., & White, S. D. M. 1985, ApJ, 292, 371
Dey, A., Bian, C., Soifer, B. T., et al. 2005, ApJ, 629, 654
Debuhr, J., Quataert, E., & Ma, C.-P. 2012, MNRAS, 420, 222
Dijkstra, M., Haiman, Z., & Spaans, M. 2006, ApJ, 649, 14
Dijkstra, M., & Loeb, A. 2009, MNRAS, 400, 1109
Dopita, M. A., & Sutherland, R. S. 1996, ApJS, 102, 161
Eisenstein, D. J., Weinberg, D. H., Agol, E., et al. 2011, AJ, 142, 72
Faucher-Giguère, C.-A., Kereš, D., Dijkstra, M., Hernquist, L., & Zaldarriaga, M. 2010, ApJ, 725, 633
Fardal, M. A., Katz, N., Gardner, J. P., et al. 2001, ApJ, 562, 605
Ferland, G. J. 1996, University of Kentucky Internal Report, 565 pages,
Francis, P. J., Williger, G. M., Collins, N. R., et al. 2001, ApJ, 554, 1001
Fumagalli, M., Prochaska, J. X., Kasen, D., et al. 2011, MNRAS, 418, 1796
Geach, J. E., Alexander, D. M., Lehmer, B. D., et al. 2009, ApJ, 700, 1
Gould, A., & Weinberg, D. H. 1996, ApJ, 468, 462
Gurzadyan, G. A. 1997, The Physics and Dynamics of Planetary Nebulae, XVI, 513 pp. 179 figs. 93 tabs.. Springer-Verlag Berlin Heidelberg New York. Also Astronomy and Astrophysics Library, 179
Kollmeier, J. A., Zheng, Z., Davé, R., et al. 2010, ApJ, 708, 1048
Heckman, T. M., Lehnert, M. D., Strickland, D. K., & Armus, L. 2000, ApJS, 129, 493
Haiman, Z., & Rees, M. J. 2001, ApJ, 556, 87
Harrison, C. M., Alexander, D. M., Swinbank, A. M., et al. 2012, MNRAS, 426, 1073
Harrison, C. M., Alexander, D. M., Mullaney, J. R., & Swinbank, A. M. 2014, MNRAS, 441, 3306

TABLE 1
PROPERTIES OF Lyα NEBULA MAMMOTH-1

Center[a]	Aperture	$L_{\rm total}$ (10^{43} erg s^{-1})	$L_{\rm nebula}$ (10^{43} erg s^{-1})
α = 14:41:27.62, δ =+40:03:31.44	Entire nebula[b]	52.8 ± 2.0	49.0 ± 1.0

a: We apply source B's position as the center of MAMMOTH-1 (see Figure 1 and Figure 2).
b: We include all the continuous area with surface brightness (SB) $> 4.8 \times 10^{-18}$ erg s^{-1} cm^{-2} arcsec^{-2}).

TABLE 2
SURFACE BRIGHTNESS OF EMISSION LINES IN MAMMOTH-1 NEBULA (BLUE APERTURES IN FIGURE 5)

Aperture	$SB_{\rm total}$ (erg s^{-1} cm^{-2} arcsec^{-2})	$SB_{\rm CIV}$ (erg s^{-1} cm^{-2} arcsec^{-2})	$SB_{\rm HeII}$ (erg s^{-1} cm^{-2} arcsec^{-2})	$SB_{\rm CIII]}$ (erg s^{-1} cm^{-2} arcsec^{-2})
2" $\times$ 1.2" (16.7 $\times$10 kpc^2)	$29.9 \pm 0.1 \times 10^{-17}$	$3.7 \pm 0.1 \times 10^{-17}$	$3.3 \pm 0.1 \times 10^{-17}$	$1.0 \pm 0.1 \times 10^{-17}$

TABLE 3
A COMPARISON BETWEEN THE Lyα NEBULA MAMMOTH-1 AND OTHER ENORMOUS Lyα NEBULAE (ELANE)

Name	$L_{\rm total}$ (10^{43} erg s^{-1})	$L_{\rm nebula}$ (10^{43} erg s^{-1})	size[a] (kpc)	Ionizing sources	$L_{\rm CIV}/L_{\rm Ly\alpha}$	$L_{\rm HeII}/L_{\rm Ly\alpha}$
MAMMOTH-1	52.8 ± 0.1	49.0 ± 1.0	≈ 440	faint source ($U = 25.8$, $B = 23.7$, $V = 24.3$, $i = 24.3$)	0.12 ± 0.01	0.12 ± 0.01
Slug[b]	143.0 $\pm$5.0	≈ 22.0	≈ 500	ultraluminous QSO	< 0.12 (2σ)	< 0.08 (2σ)
Jackpot[c]	≈ 20.0		≈ 310	QSO quartet, ultraluminous QSO		
Q0042-2627[d]	17.0		318	ultraluminous QSO	< 0.01 (2σ)	< 0.01 (2σ)
CTS G18.01 [d]	19.0		239	ultraluminous QSO	< 0.04 (2σ)	< 0.03 (2σ)

[a] We define size for a surface brightness SB$\geq 4.8 \times 10^{-18}$ erg s^{-1} cm^{-2} arcsec^{-2}. For the other Lyα nebulae, the luminosities are just cited from the published papers, without defining a surface brightness threshold.
[b]The parameters of the Slug nebula are from Cantalupo et al. (2014) and Arrigoni-Batta et al. (2015).
[c]The parameters of the Jackpot nebula are from (Hennawi et al. 2015).
[d]The parameters of the two Lyα nebulae, Q0042-2627 and CTS G18.01, are from the MUSE Lyα nebulae survey (Borisava et al. 2016).

Hernquist, L., Katz, N., Weinberg, D. H., & Miralda-Escudé, J. 1996, ApJ, 457, L51

Heckman, T. M., Miley, G. K., Lehnert, M. D., & van Breugel, W. 1991, ApJ, 370, 78

Hopkins, P. F., Hernquist, L., Cox, T. J., et al. 2005, ApJ, 630, 716

Hennawi, J. F., Prochaska, J. X., Burles, S., et al. 2006, ApJ, 651, 61

Hennawi, J. F., & Prochaska, J. X. 2013, ApJ, 766, 58

Hennawi, J. F., Prochaska, J. X., Cantalupo, S., & Arrigoni-Battaia, F. 2015, Science, 348, 779

Ho, I.-T., Kewley, L. J., Dopita, M. A., et al. 2014, MNRAS, 444, 3894

Kereš, D., Katz, N., Weinberg, D. H., & Davé, R. 2005, MNRAS, 363, 2

Leitherer, C., Schaerer, D., Goldader, J. D., et al. 1999, ApJS, 123, 3

Lee, K.-G., Hennawi, J. F., White, M., Croft, R. A. C., & Ozbek, M. 2014, ApJ, 788, 49

Martin, C. L. 2005, ApJ, 621, 227

McCarthy, P. J. 1993, ARA&A, 31, 639

Martin, D. C., Chang, D., Matuszewski, M., et al. 2014, ApJ, 786, 107

Martin, D. C., Matuszewski, M., Morrissey, P., et al. 2015, Nature, 524, 192

Matsuda, Y., Yamada, T., Hayashino, T., et al. 2005, ApJ, 634, L125

Miralda-Escudé, J., Cen, R., Ostriker, J. P., & Rauch, M. 1996, ApJ, 471, 582

Miley, G., & De Breuck, C. 2008, A&A Rev., 15, 67

Moy, E., & Rocca-Volmerange, B. 2002, A&A, 383, 46

Nesvadba, N. P. H., Lehnert, M. D., Eisenhauer, F., et al. 2006, ApJ, 650, 693

Prescott, M. K. M., Dey, A., & Jannuzi, B. T. 2009, ApJ, 702, 554

Palunas, P., Teplitz, H. I., Francis, P. J., Williger, G. M., & Woodgate, B. E. 2004, ApJ, 602, 545

Prochaska, J. X., Weiner, B., Chen, H.-W., Mulchaey, J., & Cooksey, K. 2011, ApJ, 740, 91

Prochaska, J. X., Lau, M. W., & Hennawi, J. F. 2014, ApJ, 796, 140

Rauch, M. 1998, ARA&A, 36, 267

Reuland, M., van Breugel, W., Röttgering, H., et al. 2003, ApJ, 592, 755

Rosdahl, J., & Blaizot, J. 2012, MNRAS, 423, 344

Schaerer, D. 2003, A&A, 397, 527

Steidel, C. C., Adelberger, K. L., Dickinson, M., et al. 1998, ApJ, 492, 428

Steidel, C. C., Adelberger, K. L., Shapley, A. E., et al. 2000, ApJ, 532, 170

Steidel, C. C., Adelberger, K. L., Shapley, A. E., et al. 2005, ApJ, 626, 44

Taniguchi, Y., & Shioya, Y. 2000, ApJ, 532, L13

Tombesi, F., Meléndez, M., Veilleux, S., et al. 2015, Nature, 519, 436

Tumlinson, J., Shull, J. M., & Venkatesan, A. 2003, ApJ, 584, 608

Tumlinson, J., Thom, C., Werk, J. K., et al. 2011, Science, 334, 948

Villar-Martin, M., Tadhunter, C., & Clark, N. 1997, A&A, 323, 21

Wilman, R. J., Gerssen, J., Bower, R. G., et al. 2005, Nature, 436, 227

Villar-Martín, M., Binette, L., & Fosbury, R. A. E. 1999, A&A, 346, 7

Villar-Martín, M., Sánchez, S. F., Humphrey, A., et al. 2007, MNRAS, 378, 416

Yang, Y., Zabludoff, A. I., Davé, R., et al. 2006, ApJ, 640, 539

Yang, Y., Zabludoff, A., Tremonti, C., Eisenstein, D., & Davé, R. 2009, ApJ, 693, 1579

Yang, Y., Zabludoff, A., Eisenstein, D., & Davé, R. 2010, ApJ, 719, 1654

Yang, Y., Zabludoff, A., Jahnke, K., & Davé, R. 2014, ApJ, 793, 114